Particle dynamics in quasi-isochronous storage rings

A. Riabko, M. Bai, B. Brabson, C. M. Chu, X. Kang, D. Jeon, S. Y. Lee, and X. Zhao

Department of Physics, Indiana University, Bloomington, Indiana 47405

The synchrotron equation of motion in quasi-isochronous (QI) storage rings is transformed to a universal Weierstrass equation, where the solution is given by Jacobian elliptic functions. Scaling properties of the QI Hamiltonian are derived. The effects of phase space damping and the sensitivity of particle motion to external harmonic modulation are studied. We find that the rf phase modulation is particularly enhanced in QI storage rings. Exact formula and sum rules for resonance strength coefficients are derived. When the QI dynamical system is subject to harmonic modulation, it exhibits a sequence of period-2 bifurcations leading to global chaos in a region of modulation tune. This means that the operators of QI storage rings should pay special attention to rf phase noise. [S1063-651X(96)06707-4]

PACS number(s): 29.20.Dh, 03.20.+i, 05.45.+b

I. INTRODUCTION

Very short electron bunches, e.g., submillimeter in bunch length, can be important for such applications as time resolved experiments, next generation light sources, coherent synchrotron radiation, and damping rings for the next linear colliders. A possible method for producing short bunches is to reduce the phase slip factor or the momentum compaction factor for electron storage rings. Because of its potential benefit, interest in the physics of the low-α_c lattice has recently grown [1–7].

The fractional path length difference between an off-momentum particle and the synchronous particle is related to the fractional momentum deviation by

$$\frac{\Delta C}{C_0} = \alpha_c \delta, \quad \delta = \frac{\Delta p}{p_0},$$

where C_0 and p_0 are the circumference and the momentum of the synchronous particle, and α_c is called the momentum compaction factor. Here we neglect the change of orbit length due to betatron motion.

For actual storage rings, the momentum compaction factor is a function of the fractional momentum deviation, i.e.,

$$\alpha_c = \alpha_{c0} + \alpha_{c1}\delta + \cdots.$$

In most applications, the expansion can be truncated at the second term because the higher order terms are small. Including the velocity difference between the off-momentum particle and the synchronous particle, the fraction deviation of the revolution frequency is given by

$$\frac{\Delta \omega}{\omega_0} = -\eta\delta, \quad (1.1)$$

with the phase slip factor

$$\eta = \eta_0 + \eta_1\delta + \cdots, \quad (1.2)$$

where η_0 and η_1 are the first order and the second order phase slip factors. In realistic storage rings, the truncation of the phase slip factor at the η_1 term is a good approximation.

Because the velocity difference between electrons in a storage ring is very small, all η_i's are equal to α_{ci}'s.

For nominal storage rings, where $|\eta_1\delta| \ll |\eta_0|$, the synchrotron motion is dominated by the η_0 term, where particles are grouped together into bunches inside stable rf buckets. For small bunches inside the bucket, the bunch width is proportional to $\sqrt{|\eta_0|}$ (see Appendix A). Thus a short bunch regime is equivalent to the condition of a small $|\eta_0|$. Since η is related to the the revolution frequency deviation [see Eq. (1.1)], the condition of small $|\eta|$ is also called the isochronous condition or quasi-isochronous (QI) condition. A lattice which provides the QI condition is called a QI lattice. For electron storage rings, the QI condition is equivalent to a small momentum compaction.

In the past few years, many low-α_c experiments were performed [6]. These experiments showed that bunch lengths were smaller for low-α_c lattices. However, the total stored beam current was also small. At the high current limit, these experiments also showed that the bunch lengths were determined mainly by the potential well distortion resulting from a broadband impedance. Although experiments have not yet determined the benefits of a QI lattice, a better understanding of the particle dynamics in the QI Hamiltonian system may well be the source of future innovation. Furthermore, in an experiment at the advanced light source (ALS) at the Lawrence Berkeley National Laboratory, beams in the QI condition were observed to split into satellite bunches [7]. What causes the beam to split into beamlets? What is the sensitivity of the QI lattice to external perturbation such as rf phase noise?

This paper studies synchrotron motion at or near the QI condition. We will study the sensitivity of the Hamiltonian system under harmonic modulation. In Sec. II we will show that the QI synchrotron Hamiltonian can be transformed to a universal Weierstrass equation, which is independent of the rf voltage, synchronous phase angle, energy, η_0, and η_1. The solution for the particle motion in this universal QI Hamiltonian is given by the Weierstrass $\wp$ function or the Jacobian elliptic function [8,9]. Properties of this universal QI Hamiltonian will be discussed. The increase in the stable phase space area due to phase space damping will also be addressed. Section III discusses the effect of rf noise on par-
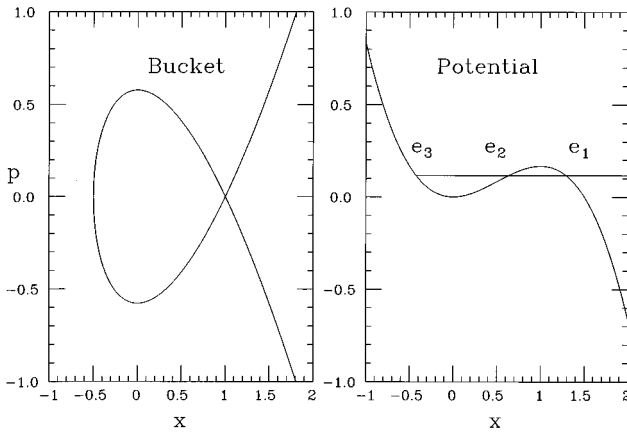
FIG. 1. The rf bucket (left plot) and the potential (right plot) for the normalized QI Hamiltonian. Three turning points e_1, e_2, and e_3 are also marked. Note here that the coordinate x is associated with the momentum deviation δ and the ordinate p is proportional to the phase coordinate ϕ.

ticle motion. In the presence of harmonic phase modulation, parametric resonances will be identified. We will show that the phase space can become chaotic with relatively weak modulation. In the presence of strong damping with moderate harmonic modulation, the system undergoes a sequence of period-2 bifurcation en route towards strange chaotic attractors. Based on our systematic study, some beam dynamics experiments will also be suggested in Sec. IV. The conclusion is given in Sec. V.

II. PARTICLE HAMILTONIAN IN QI STORAGE RINGS

For synchrotron storage rings operating near the isochronous condition, the phase slip factor is given by Eq. (1.2), and the small amplitude synchrotron tune is given by

$$\nu_s = \sqrt{\frac{heV|\eta_0 \cos\phi_s|}{2\pi\beta^2 E_0}}, \tag{2.1}$$

where h, V, and ϕ_s are the harmonic number, rf voltage, and the synchronous phase angle, respectively, and βc and E_0 are the velocity and the energy of the beam. Using $t = \nu_s \theta$ as the time variable, where $\theta = s/R$ is the orbiting angle, and using (x,p) as the conjugate phase space coordinates, where

$$x = -\frac{\eta_1}{\eta_0}\frac{\Delta p}{p_0}, \quad p = \frac{dx}{dt}, \tag{2.2}$$

the synchrotron Hamiltonian for particle motion in QI storage rings is given by (see Appendix A)

$$H = \frac{1}{2}p^2 + \frac{1}{2}x^2 - \frac{1}{3}x^3. \tag{2.3}$$

The ''energy'' E of the autonomous Hamiltonian is a constant of motion with $E \in [0, \frac{1}{6}]$ for particles inside the bucket. Figure 1 shows the potential energy and the stable bucket area for the Hamiltonian. The bucket is plotted sideways so that the corresponding potential energy has a similar coordi-

TABLE I. Parametric range of the Weierstrass $\wp$ function.

E	0	1/12	1/6
ξ	0	30°	60°
e_1	3/2	$(1+\sqrt{3})/2$	1
e_2	0	$\frac{1}{2}$	1
e_3	0	$(1-\sqrt{3})/2$	$-1/2$
m	0	1/2	1

nate x. We use x to represent the normalized coordinate of Eq. (2.2) because it is related to the radial closed orbit.

The equation of motion for a particle with energy E is given by

$$\left(\frac{dx}{dt}\right)^2 = \frac{2}{3}x^3 - x^2 + 2E. \tag{2.4}$$

Letting $u = t/\sqrt{6}$ and $\wp = x$, the equation of motion is transformed to the standard Weierstrass equation [9]:

$$\left(\frac{d\wp(u)}{du}\right)^2 = 4(\wp - e_1)(\wp - e_2)(\wp - e_3), \tag{2.5}$$

where the turning points, $e_1 \geq e_2 \geq e_3$, are given by

$$e_1 = \frac{1}{2} + \cos(\xi), \quad e_2 = \frac{1}{2} + \cos(\xi - 120°),$$

$$e_3 = \frac{1}{2} + \cos(\xi + 120°),$$

$$\xi = \frac{1}{3}\arccos(1 - 12E).$$

Table I lists the ranges of interest for relevant parameters of this dynamical system. Figure 1 shows the bucket area and the potential energy as a function of x, which is proportional to the fractional momentum deviation of the synchronous particle.

The Weierstrass elliptic $\wp$ function is a single valued doubly periodic function of a single complex variable. For particles inside the separatrix, the discriminant is positive, i.e., $\Delta = 648E(1 - 6E) > 0$, and the Weierstrass $\wp$ function can be expressed in terms of the Jacobian elliptic function (see Appendix B):

$$x(t) = e_3 + (e_2 - e_3)\text{sn}^2\left(\sqrt{\frac{e_1 - e_3}{6}}t \,\middle|\, m\right), \tag{2.6}$$

$$m = \frac{e_2 - e_3}{e_1 - e_3} = \frac{\sin\xi}{\sin(\xi + 60°)} \leq 1. \tag{2.7}$$

Here the Jacobian elliptic function is defined as

$$\sin(v|m) = \sin w, \quad v = \int_0^w \frac{dz}{\sqrt{1 - m\sin^2 z}}. \tag{2.8}$$

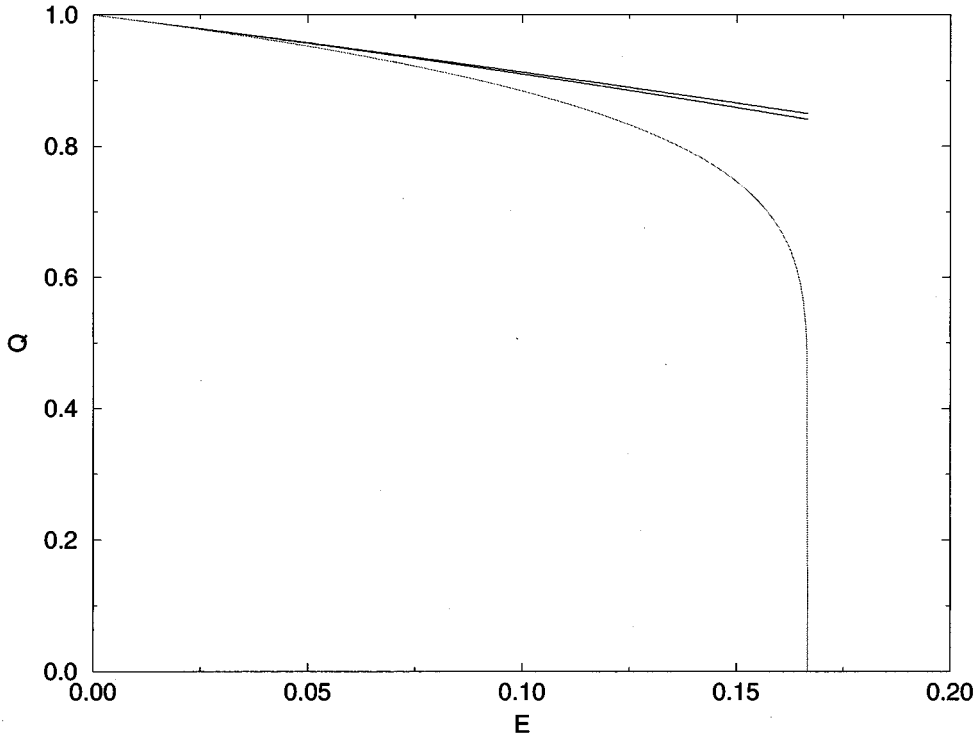The period and the tune of the elliptic function are given by

FIG. 2. $Q(E)$ vs E. The first order and the second order detuning terms of Eq. (2.18) are also shown. Because of the sharp drop of the synchrotron tune $Q(E)$ around the separatrix, parametric resonances of all orders overlap with each other near the separatrix trajectory and give rise to stochasticity.

$$T = 2\sqrt{6}\frac{K(m)}{\sqrt{e_1 - e_3}}, \quad Q = \frac{2\pi}{T} = \frac{\pi[\sqrt{3}\sin(\xi + 60°)]^{1/2}}{\sqrt{6}K(m)}. \tag{2.9}$$

Figure 2 shows $Q(E)$ as a function of energy. At the center of the bucket, where $E = 0$, we have $Q = 1$ and at the separatrix, where $E = \frac{1}{6}$, we have $Q = 0$. In the original accelerator coordinate system, the synchrotron tune becomes

$$Q_s = \nu_s \frac{\pi[\sqrt{3}\sin(\xi + 60°)]^{1/2}}{\sqrt{6}K(m)}. \tag{2.10}$$

Thus the small amplitude synchrotron tune is ν_s. In particular, we note that the synchrotron tune decreases to zero very sharply near the separatrix. Because of the sharp decrease in synchrotron tune near the separatrix, parametric resonances induced by the time-dependent perturbation overlap one another and give rise to chaos.

A. Nonlinear detuning parameter

Substituting the ansatz for a small amplitude expansion

$$x = \sqrt{2J}\cos\psi \tag{2.11}$$

into the Hamiltonian, where (J, ψ) are approximate action-angle variables, we obtain

$$H = J - \frac{1}{3}(2J)^{3/2}\cos^3\psi. \tag{2.12}$$

Using the generating function

$$F_2(\bar{J}, \psi) = \bar{J}\psi + \frac{1}{12}(2\bar{J})^{3/2}\left(\frac{1}{3}\sin 3\psi + 3\sin\psi\right), \tag{2.13}$$

we obtain

$$J = \frac{\partial F_2(\bar{J}, \psi)}{\partial\psi} = \bar{J} + \frac{1}{3}(2\bar{J})^{3/2}\cos^3\psi, \tag{2.14}$$

and the new Hamiltonian becomes

$$H = \bar{J} + \frac{1}{3}(2\bar{J})^{3/2}\cos^3\psi - \frac{1}{3}(2J)^{3/2}\cos^3\psi. \tag{2.15}$$

Expanding the Hamiltonian to the second order in the new action variable $\bar{J}$, the time averaged Hamiltonian becomes

$$\langle H\rangle_{\bar{\psi}} = \bar{J} - \frac{4}{3}\bar{J}^2\langle\cos^6\bar{\psi}\rangle_{\bar{\psi}} = \bar{J} - \frac{\alpha}{2}\bar{J}^2, \tag{2.16}$$

where $\alpha = \frac{5}{6}$ is the detuning parameter. It is worth pointing out that the detuning parameter is larger than that of the nominal rf Hamiltonian, where $\alpha = \frac{1}{8}$ (see, e.g., Refs. [12,13]). The most important difference between the tunes of the QI Hamiltonian system and the nominal rf pendulum Hamiltonian is the behavior of the tunes at large amplitude oscillations near the separatrix.

Performing canonical perturbation calculation to the next order, the detuning parameter becomes

$$H = \bar{J} - \frac{5}{12}\bar{J}^2 - \frac{77}{864}\bar{J}^3, \tag{2.17}$$

or equivalently, the tune is given by

$$Q = 1 - \frac{5}{6}\bar{J} - \frac{77}{288}\bar{J}^2. \tag{2.18}$$

Figure 2 plots $Q(E)$ vs E, where the first order detuning and the second order detuning are shown. Note here that the first order detuning is a good approximation to the synchrotron tune for $E \leq 1/12$, yet the second order detuning parameter does not improve the approximation beyond $E > 1/12$.

B. Action-angle variables

The action of a Hamiltonian torus is defined as

$$J = \frac{1}{2\pi} \oint p \, dx = \frac{1}{\pi} \sqrt{\frac{2}{3}} \int_{e_3}^{e_2} \sqrt{(e_1 - x)(e_2 - x)(x - e_3)} \, dx. \tag{2.19}$$

Since the Hamiltonian torus can be described by $x = e_3 + (e_2 - e_3) \sin^2 w$, we have (Formula 3.671 of Ref. [10])

$$J = \frac{2}{\pi} \sqrt{\frac{2}{3}} (e_2 - e_3)^2 (e_1 - e_3)^{1/2}$$

$$\times \int_0^{\pi/2} \sin^2 w \cos^2 w \sqrt{1 - m \sin^2 w} \, dw$$

$$= \frac{1}{8} \sqrt{\frac{2}{3}} (e_2 - e_3)^2 (e_1 - e_3)^{1/2} F\left(\frac{3}{2}, -\frac{1}{2}; 3; m\right), \tag{2.20}$$

where hypergeometric function F is given by [9]

$$F\left(\frac{3}{2}, -\frac{1}{2}; 3; m\right) = 1 - \frac{1}{4}m - \frac{5}{128}m^2 - \frac{7}{512}m^3 - \cdots. \tag{2.21}$$

Using the generating function

$$F_2(x, J) = \int_{e_3}^{x} p \, dx, \tag{2.22}$$

the angle variable is given by

$$\psi = \frac{\partial F_2}{\partial J} = \sqrt{\frac{6}{e_1 - e_3}} Q F(w|m) = Qt, \tag{2.23}$$

where $Q(J) = dH/dJ$ is the amplitude-dependent synchrotron tune given by Eq. (2.9), and $F(w|m)$ is the incomplete elliptic integral given by

$$F(w|m) = \int_0^w \frac{dz}{\sqrt{1 - m \sin^2 z}}, \quad w = \arcsin \sqrt{\frac{x - e_3}{e_2 - e_3}}, \tag{2.24}$$

with modulo m of Eq. (2.7).

C. The separatrix orbit and the bucket area

The maximum action of the bounded motion is given by

$$J_{sep} = \frac{1}{2\pi} \oint_{sep} p \, dx = \frac{3}{5\pi}. \tag{2.25}$$

Thus the bucket area of the (ϕ, δ) phase space is given by (see Appendix A)

$$\mathcal{A}_B = \frac{6}{5} \left(\frac{|\eta_0|^{5/2}}{|\eta_1|^2} \right) \left(\frac{2\pi h \beta^2 E}{eV |\cos\phi_s|} \right)^{1/2}. \tag{2.26}$$

In contrast to the nominal synchrotron Hamiltonian, the bucket area of the QI Hamiltonian increases with *decreasing* rf voltage V and $|\cos\phi_s|$. Note also that the bucket area is proportional to $|\eta_0|^{5/2}/|\eta_1|^2$. For a lattice with a small η_0, a proper correction for η_1 becomes necessary in order to provide a stable phase space for the beam bunch.

The separatrix orbit, which corresponds to $m = 1$, is given by

$$x(t) = 1 - \frac{3}{\cosh t + 1}, \quad p(t) = \frac{3 \sinh t}{(\cosh t + 1)^2}, \tag{2.27}$$

where the phase space for the bounded motion is limited by

$$x \in \left[-\frac{1}{2}, 1 \right], \quad p \in \left[-\frac{1}{\sqrt{3}}, \frac{1}{\sqrt{3}} \right].$$

This means that the maximum tolerable momentum width is given by

$$\hat{\delta} = \frac{|\eta_0|}{2|\eta_1|}. \tag{2.28}$$

However, we must keep in mind that the damping coefficient is also enhanced for a QI lattice. Due to the synchrotron radiation damping, the equation of motion for QI storage rings is given by (see Appendix A)

$$x'' + Ax' + x - x^2 = 0, \tag{2.29}$$

where

$$A = \frac{\lambda}{\nu_s} = \frac{U_0 J_E}{2\pi E_0 \nu_s} \tag{2.30}$$

is the effective damping coefficient with the damping decrement λ. Table III in Appendix A lists values for damping coefficient A for some non-QI storage rings. For QI storage rings, the effective damping coefficient is enhanced by the corresponding decrease in the synchrotron tune, where the value of A may vary from 0 to 0.5.

Including the damping term, the basin of attraction which damps to a stable fixed point (SFP) is enlarged. Figure 3 shows the basin of attraction for the damping coefficients $A = 0, 0.2, 0.5$, respectively. A practitioner's *definition* of the "stable phase space area" (bucket area) is the phase space area that damps to the fixed point attractor and is bounded by the line $x \leq 1$ or $\Delta p/p_0 \leq |\eta_0|/|\eta_1|$. The right plot of Fig. 3 shows the "bucket area" enhancement factor as a function
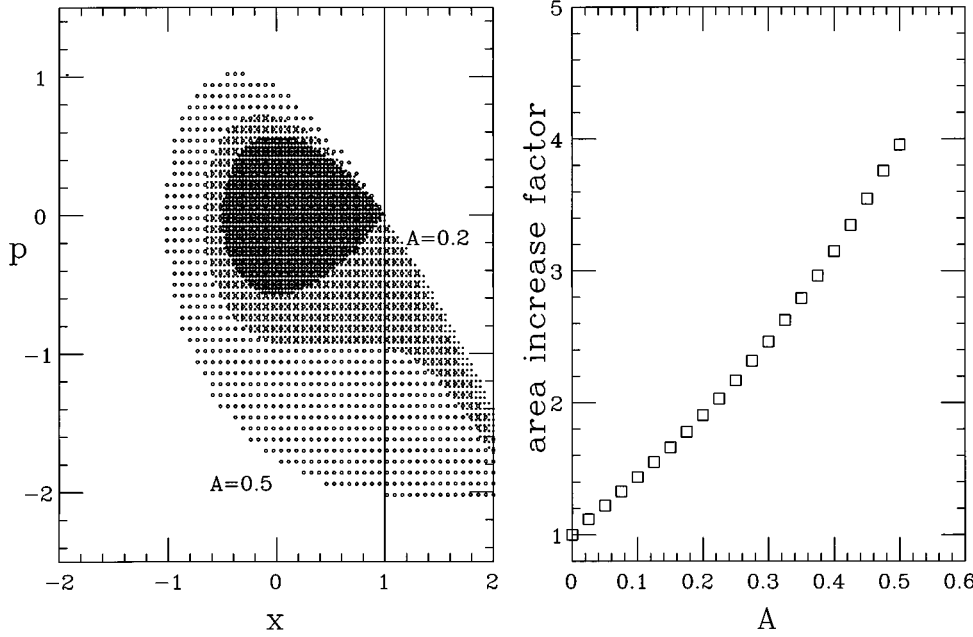
FIG. 3. The stable phase space area with the effective damping coefficients $A = 0$, 0.2, 0.5 is shown in the left graph with different shades. We define the operational ''bucket area'' as the stable phase area bounded by the $x \lesssim 1$. The bucket area enhancement factor, defined as the ratio of the stable phase space areas with and without damping, is plotted as the function of the damping coefficient A on the right plot.

of the damping parameter A. Here the enhancement factor is the ratio of the ''bucket areas'' with and without damping.

The shape of the attractor basin can be understood as follows. Consider the basin of attraction with the damping parameter $A = 0.5$. The particle on the limiting trajectory along the ''separatrix,'' clockwise in (x,p) phase space, experiences damping towards the center of the bucket. Its ''energy'' is gradually reduced along its trajectory. As it reaches the ''unstable fixed point'' of the undamped Hamiltonian system, its energy is equal to that of the separatrix orbit without damping, i.e., $E = \frac{1}{6}$. This feature seems to be independent of the magnitude of the damping parameter shown in the left plot of Fig. 3. Using this property, we can estimate the increase in phase space area as follows.

First, we launch a particle from the unstable fixed point (UFP) at $(p = 0, \ x = 1)$ and let the particle move along the separatrix (limiting trajectory) counterclockwise. Instead of damping, the particle gains energy due to the reverse motion. The amount of energy gained is given by

$$\Delta E \approx A \int_{-\infty}^{\infty} p^2(t) dt = \frac{6}{5} A, \qquad (2.31)$$

where the separatrix trajectory of Eq. (2.27) is used. Thus the equivalent energy of the limiting trajectory is $E_{eq} = \frac{1}{6} + \frac{6}{5} A$. We now estimate the bucket area of the limiting trajectory as the area enclosed by the particle trajectory with an equivalent energy E_{eq}, i.e.,

$$\mathcal{A}(E_{eq}) \approx \oint_{x \lesssim 1} p \, dx = \frac{6}{5} + \sqrt{3} \left[\left(1 + \frac{36}{5} A \right)^{1/2} - 1 \right]$$

$$\times \left(1 + \frac{16}{15} A \right). \qquad (2.32)$$

Thus the bucket area enhancement factor is approximately given by

$$\mathcal{F} \approx 1 + \frac{5\sqrt{3}}{6} \left[\left(1 + \frac{36}{5} A \right)^{1/2} - 1 \right] \left(1 + \frac{16}{15} A \right), \quad (2.33)$$

which agrees with numerical simulations shown in the right plot of Fig. 3.

D. Expansion of phase space coordinates and sum rules

Expansion of phase space coordinates in action-angle variables is important in obtaining essential characteristics of particle motion. Since $x(t)$ is an even function of t or ψ, we obtain

$$x(t) = g_0 + \sum_{n=1}^{\infty} g_n \cos(n\psi), \qquad (2.34)$$

where

$$g_0 = e_3 + (e_1 - e_3) \frac{K(m) - E(m)}{K(m)},$$

$$g_n = (e_1 - e_3) \frac{2\pi^2}{K^2(m)} \frac{(-1)^n n q^n}{1 - q^{2n}}, \qquad (2.35)$$

with

$$q = e^{-\pi K'/K} = \frac{m}{16} + 8 \left(\frac{m}{16} \right)^2 + 84 \left(\frac{m}{16} \right)^3 + \cdots,$$

$$\psi = \frac{\pi}{2K} \sqrt{\frac{e_1 - e_3}{6}} \nu_s \theta = Q \nu_s \theta = Q t,$$

where $K(m)$ and $E(m)$ are the complete elliptic integrals of the first and second kind, respectively. Similarly, the expansion of p becomes

$$p = \frac{dx}{dt} = -Q \sum_{n=1}^{\infty} n g_n \sin n\psi, \qquad (2.36)$$

where $Q = Q(J)$ is the tune of the system. It is worth noting that the expansion of the coordinate x contains all harmonics. This differs from the similar expansion in the nominal rf Hamiltonian, where only odd harmonics are present. Since $g_n \sim n q^n$ at small q, all g_n coefficients are zero at the center of the bucket where $J = 0$. Near the center of the bucket, where q is a very small number, the motion is dominated by the $n = 1$ and $n = 2$ harmonics, i.e., the dipole and quadrupole modes. If external phase modulation is applied to the system, the system will execute dipole and quadrupolelike oscillations that will be discussed in the next section. Figure 4 shows the Fourier amplitudes g_0, g_1, g_2 and the parameter q as a function of E. Because the g_1 and g_2 of nearby harmonics are large, they may interact coherently to give rise to higher order parametric resonances.

The expansion coefficients of Eq. (2.34) satisfy the sum rules (see Appendix C)

$$S_p(J) = \frac{1}{2\pi} \int p^2 d\psi = QJ = \frac{Q^2}{2} \sum_{n=1}^{\infty} n^2 g_n^2, \quad (2.37)$$

$$S_x(J) = \frac{1}{2\pi} \int x^2 d\psi = g_0^2 + \frac{1}{2} \sum g_n^2 = g_0, \quad (2.38)$$

or equivalently

$$\sum_{n=1}^{\infty} g_n^2(J) = 2g_0(1 - g_0). \quad (2.39)$$

Since $g_0 = 1$ on the separatrix, the strength of all harmonics must vanish on the separatrix orbit. Because $\sum_{n=1}^{\infty} n^2 g_n^2$ diverges at $J = J_{\text{sep}}$, g_n decreases slowly with respect to the mode number n near the separatrix.

III. PARTICLE DYNAMICS WITH PHASE MODULATION

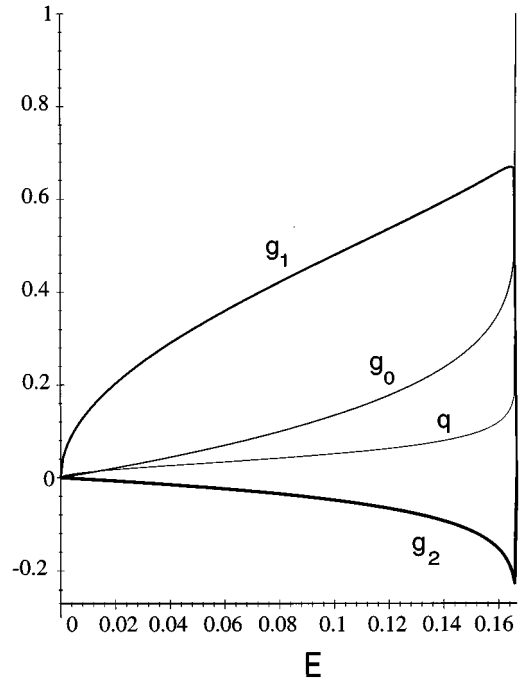In the presence of the phase modulation, the Hamiltonian in the normalized phase space coordinates is given by

FIG. 4. The strength functions g_0, g_1, g_2 and the parameter q are plotted as a function of E.

$$H = \frac{p^2}{2} + \frac{1}{2}x^2 - \frac{1}{3}x^3 + \omega_m B x \cos\omega_m t, \quad (3.1)$$

where the effective modulation amplitude is

$$B = \frac{\eta_1 a}{\eta_0 \nu_s}, \quad (3.2)$$

$\omega_m = \nu_m / \nu_s$ is the normalized modulation tune, and a and ν_m are the rf phase modulation amplitude and the modulation tune in the original accelerator coordinate system, respec-
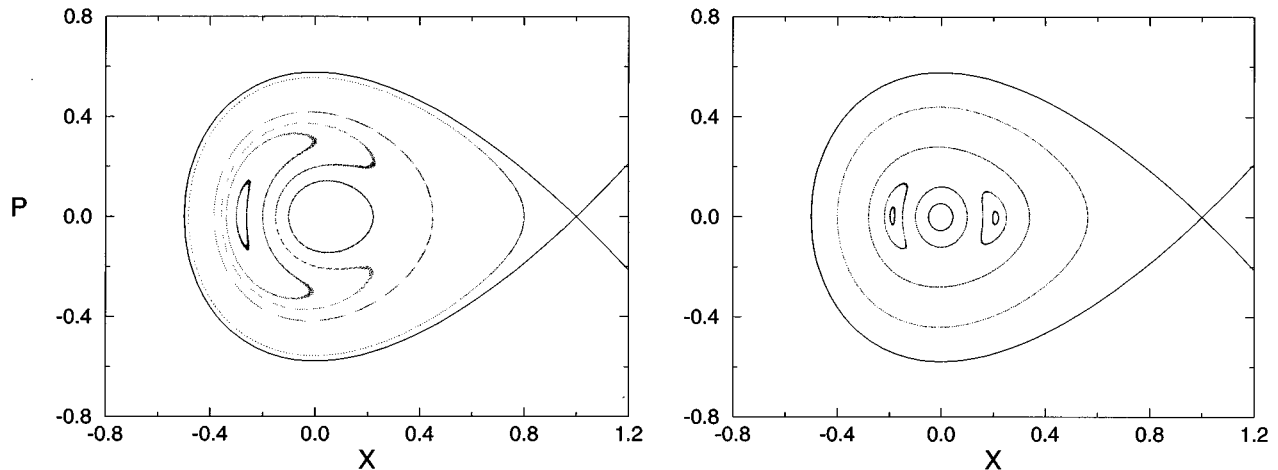

FIG. 5. The Poincaré surfaces of section for a QI Hamiltonian with $B = 0.003$ and $\omega_m = 0.96$ for the left plot and $B = 0.0055$ and $\omega_m = 1.97$ for the right plot. Here B and ω_m are rf phase modulation amplitudes and tunes, respectively. The separatrix trajectory is shown in this case for marking the boundary of stable motion of the unperturbed Hamiltonian. In reality, the separatrix is destroyed by the harmonic modulation.

tively. Because $|B| \sim |\eta_0|^{-3/2}$, the effective modulation amplitude B is greatly enhanced for QI storage rings.

Including the damping force, the equation of motion becomes

$$x'' + Ax' + x - x^2 = -\omega_m B \cos\omega_m t, \qquad (3.3)$$

where the effective damping coefficient A is given by Eq. (2.30). This section discusses the effects of rf phase modulation.

A. Parametric resonances and periodic solutions

First, we will discuss the equation of motion in the absence of the friction force, where the Hamiltonian with phase modulation can be expressed as

$$H = H_0(J) + \frac{1}{2}\sum_{n=1}^{\infty} \omega_m B g_n(J)[\cos(n\psi - \omega_m t) + \cos(n\psi + \omega_m t)]. \qquad (3.4)$$

When the modulation frequency is near a synchrotron harmonic, e.g., $\omega_m \approx nQ(J)$, Hamiltonian tori will be coherently perturbed by the resonance term due to the stationary phase condition. Transforming the Hamiltonian into the resonance rotating frame with the generating function

$$F_2 = \left(\psi - \frac{\omega_m}{n}t\right)J_1,$$

the *time averaged* Hamiltonian in the resonance rotating frame becomes

$$\langle H_1 \rangle = H(J_1) - \frac{\omega_m}{n}J_1 + h_n(J_1)\cos(n\psi_1). \qquad (3.5)$$

Since the effective resonance strength $h_n(J) = \frac{1}{2}\omega_m B g_n(J)$ is proportional to g_n, the expansion coefficients of the phase space coordinate in Eq. (2.34) are called the resonance strength function. There are n stable and n unstable fixed points for the resonance Hamiltonian Eq. (3.5) given by

$$\sin n\psi_{1\text{FP}} = 0, \quad \omega_m = nQ(J_{1\text{FP}}) \pm n\frac{dh_n}{dJ}\Big|_{J=J_{1\text{FP}}}. \quad (3.6)$$

Figure 5 shows Poincaré surfaces of section with parameters $(B,\omega_m) = (0.003, 0.96)$ and $(0.0055, 1.97)$, respectively. Note here that the Poincaré surface of section at $\omega_m \approx 1$ shows two resonance islands. These two resonance islands rotate around the center of the bucket with tune $Q(J_{\text{FP}})$. At $\omega_m \approx 2$, there are two outer resonance islands and one inner resonance island shown on the right plot of Fig. 5. These two outer resonance islands rotate about the center of the phase space at a tune of $\omega_m/2$.

In the presence of a weak damping force, SFPs of parametric resonances turn into attractors. Figure 6 shows the basin of attraction for the SFPs with parameters $B = 0.06$, $\omega_m = 0.86$, and $A = 0.05$ obtained from tracking 150×150 particles with an initial uniform distribution in the phase space. Note that the boundary of the basin of attraction exhibits fractal structure. Since orbits near the separatrix can easily be destroyed, many phase space points near the separatrix become unstable in the presence of weak modulation.

1. Mechanism for higher order resonances

The Hamiltonian in Eq. (3.4) is composed of a web of primary parametric resonances. If the strengths of these primary parametric resonances are large, they can interact coherently to generate a series of secondary parametric resonances [11]. Figure 7 shows the Poincaré surface of section for $\omega_m = 1.45$ and $B = 0.065$. We note that there are three
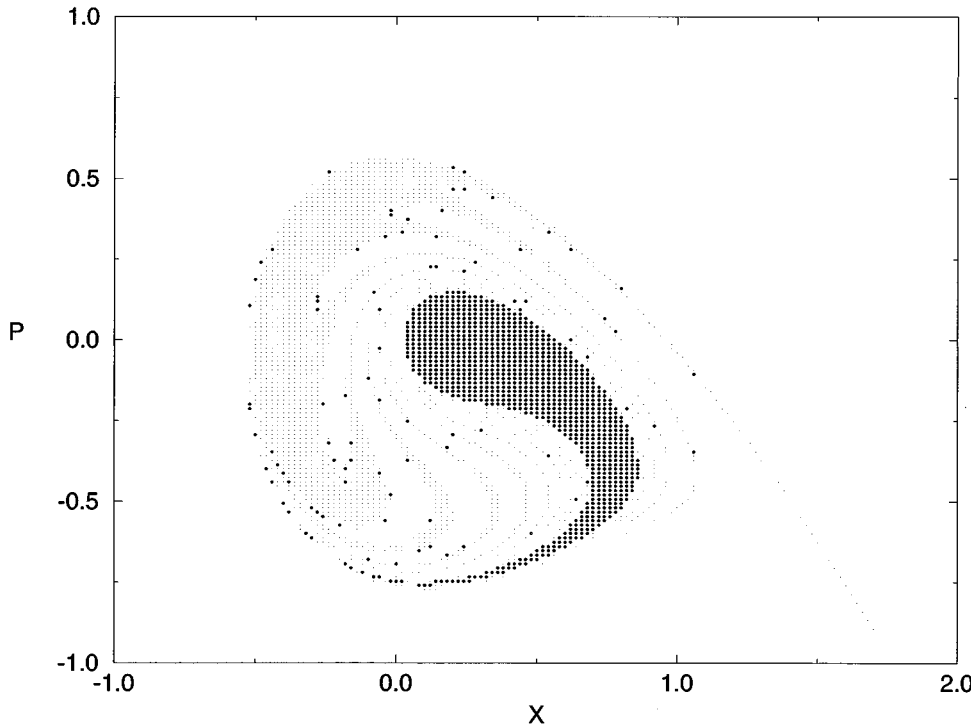

FIG. 6. The basin of attraction for a QI dynamics system with parameters $A = 0.05$, $B = 0.06$, and $\sigma_m = 0.86$, obtained from numerical simulations with 150×150 particles uniformly distributed in the phase space. All lightly shaded particles will damp to the outer attractor, and all particles with the darker shade will coverge to the inner attractor. Other particles in the phase space are lost. Note particularly that the fractal struture appears at the boundary of the basin of attraction.
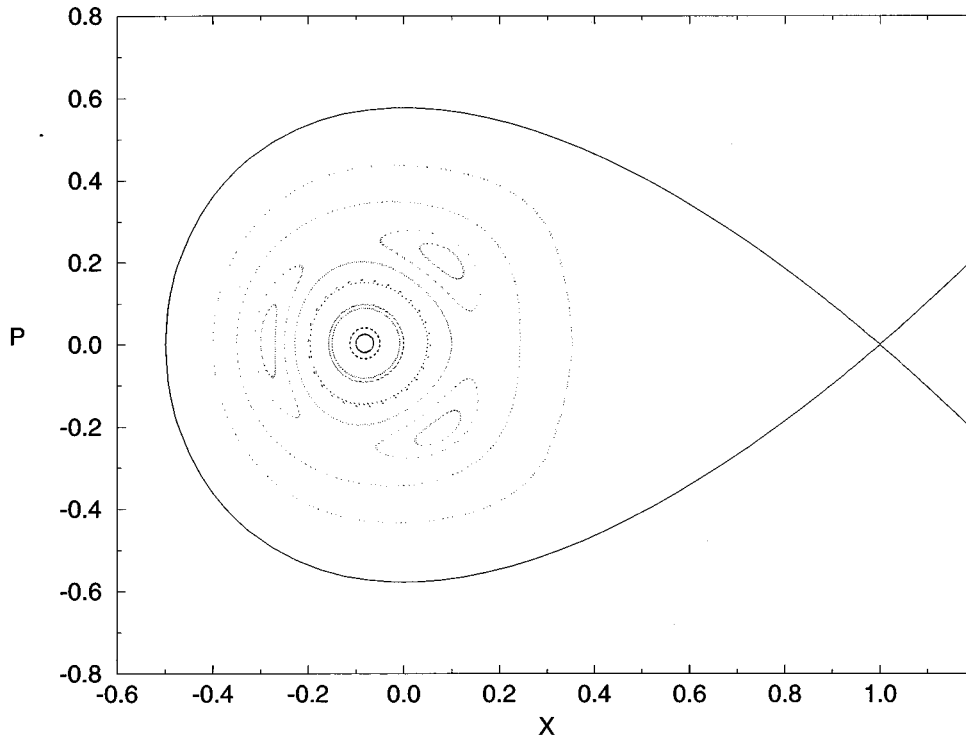
FIG. 7. Poincaré surfaces of section for a QI Hamiltonian with $B=0.065$, $\omega_m=1.45$. The secondary resonance arises from the interaction of 1:1 and 2:1 primary parametric resonances.

outer resonance islands and one inner resonance island which should appear at $\omega_m \approx 3$. To understand the origin of secondary parametric resonances, we will study the truncated Hamiltonian with two neighboring harmonics and discuss the mechanism for secondary parametric resonances based on the canonical perturbation method.

We consider the case where $n_2 Q(J) \lesssim \omega_m \lesssim n_1 Q(J)$. The Hamiltonian of Eq. (3.4) is dominated by n_1:1 and n_2:1 resonances and can be approximated by

$$H \approx E(J) + h_{n_1}(J)\cos(n_1\psi - \omega_m t) + h_{n_2}(J)\cos(n_2\psi - \omega_m t),$$
(3.7)

where n_1 and n_2 are neighboring harmonics. Using the generating function

$$W_2(\psi,\overline{J}) = \psi\overline{J} + F_{n_1}(\overline{J})\sin(n_1\psi - \omega_m t)$$

$$+ F_{n_2}(\overline{J})\sin(n_2\psi - \omega_m t),$$
(3.8)

the new action-angle variables $(\overline{\psi},\overline{J})$ are related to (ψ,J) by

$$J = \overline{J} + n_1 F_{n_1}(\overline{J})\cos(n_1\psi - \omega_m t)$$

$$+ n_2 F_{n_2}(\overline{J})\cos(n_2\psi - \omega_m t),$$

$$\overline{\psi} = \psi + F'_{n_1}(\overline{J})\sin(n_1\psi - \omega_m t) + F'_{n_2}(\overline{J})\sin(n_2\psi - \omega_m t).$$
(3.9)

The new Hamiltonian becomes

$$\overline{H} = E(\overline{J}) + \{[(n_1 Q - \omega_m)F_{n_1} + h_{n_1}(\overline{J})]\cos(n_1\overline{\psi} - \omega_m t) + [(n_2 Q - \omega_m)F_{n_2} + h_{n_2}(\overline{J})]\cos(n_2\overline{\psi} - \omega_m t)\}$$

$$+ \frac{1}{2}\frac{\partial Q}{\partial\overline{J}}[n_1 F_{n_1}\cos(n_1\overline{\psi} - \omega_m t) + n_2 F_{n_2}\cos(n_2\overline{\psi} - \omega_m t)]^2 + \left[\frac{\partial h_{n_1}}{\partial\overline{J}}\cos(n_1\overline{\psi} - \omega_m t) + \frac{\partial h_{n_2}}{\partial\overline{J}}\cos(n_2\overline{\psi} - \omega_m t)\right]$$

$$\times [n_1 F_{n_1}\cos(n_1\overline{\psi} - \omega_m t) + n_2 F_{n_2}\cos(n_2\overline{\psi} - \omega_m t)],$$
(3.10)

where we used $\psi \approx \overline{\psi}$. By setting $F_{n_1} = -h_{n_1}(\overline{J})/(n_1 Q - \omega_m)$ and $F_{n_2} = -h_{n_2}(\overline{J})/(n_2 Q - \omega_m)$, the Hamiltonian due to the second order perturbation becomes

$$\overline{H} = E(\overline{J}) + \left(\frac{1}{2}\frac{\partial Q}{\partial\overline{J}}n_1^2 F_{n_1}^2 + \frac{\partial h_{n_1}}{\partial\overline{J}}n_1 F_{n_1}\right)\cos^2(n_1\overline{\psi} - \omega_m t) + \left(\frac{1}{2}\frac{\partial Q}{\partial\overline{J}}n_2^2 F_{n_2}^2 + \frac{\partial h_{n_2}}{\partial\overline{J}}n_2 F_{n_2}\right)\cos^2(n_2\overline{\psi} - \omega_m t) + \left(\frac{\partial Q}{\partial\overline{J}}n_1 n_2 F_{n_1}F_{n_2}\right.$$

$$\left. + \frac{\partial h_{n_1}}{\partial\overline{J}}n_2 F_{n_2} + \frac{\partial h_{n_2}}{\partial\overline{J}}n_1 F_{n_1}\right)\cos(n_1\overline{\psi} - \omega_m t)\cos(n_2\overline{\psi} - \omega_m t).$$
(3.11)

Near the resonance condition at $\omega_m \approx 1/2(n_1+n_2)Q(J)$, the Hamiltonian can be approximated by

$$\bar{H} \approx E(\bar{J}) + \tilde{h}_{(n_1+n_2)}\cos[(n_1+n_2)\bar{\psi} - 2\omega_m t], \quad (3.12)$$

where

$$\tilde{h}_{(n_1+n_2)} = \frac{1}{2}\frac{\partial Q}{\partial \bar{J}}n_1 n_2 F_{n_1}F_{n_2} + \frac{1}{2}\frac{\partial h_{n_1}}{\partial \bar{J}}n_2 F_{n_2}$$

$$+ \frac{1}{2}\frac{\partial h_{n_2}}{\partial \bar{J}}n_1 F_{n_1}$$

is the effective resonance strength for the secondary $(n_1+n_2):2$ resonance. Possible secondary resonances from parent 1:1 and 2:1 parametric resonances are listed as follows:

$$\begin{array}{cccc} & 3{:}2 & 5{:}3 & 7{:}4 & 9{:}5\cdots \\ (1{:}1)+(2{:}1)\rightarrow & 4{:}3 & 6{:}4 & 8{:}5 & 10{:}6\cdots \\ & 5{:}4 & 7{:}5 & 9{:}6\cdots \end{array}$$

Here, the 3:2 resonance shown in Fig. 7 is the lowest order secondary parametric resonance. Because these parametric resonances overlap with each other, they can be easily destroyed by the strong damping. However, they provide a stochastic background for this dynamical system.

2. Harmonic linearization method and periodic solutions

The Hamiltonian formalism is not applicable when the damping parameter A of Eq. (3.3) becomes large. The attractor solutions or the periodic solutions can be obtained by the harmonic linearization method [14]. Let the ansatz of Eq. (3.3) be given by

$$x = X_0 + X_1\cos(\omega_m t + \chi_1).$$

Substituting the ansatz into Eq. (3.3) and keeping only the first harmonic in the expansion, we obtain

$$\omega_m^2 B^2 = A^2\omega_m^2 X_1^2 + (\omega_m^2 - \sqrt{1-2X_1^2})^2 X_1^2, \quad (3.13)$$

with $\tan\chi_1 = -\omega_m A/(\omega_m^2 - \sqrt{1-2X_1^2})$ and $X_0 = (1 - \sqrt{1-2X_1^2})/2$. In the weak damping and small modulation amplitude approximation, the modulation amplitude is related to modulation tune by $\omega_m \approx 1 - \frac{1}{2}X_1^2$. This result agrees well with that of Eq. (3.6) for the $n=1$ mode. Amplitudes of attractors obtained from numerical simulations are shown in the upper plot of Fig. 8, where $A=0.1$ and $B=0.1$ (square) and 0.3 (circle), respectively. The lower plot shows the amplitude of attractors for $B=0.5$ and $A=0.5$. Solid lines show the solution of Eq. (3.13), which matches with the attractor amplitude obtained from numerical simulations. In particular, if the modulation amplitude is large, there are regions of tune space where attractors will cease to exist and subharmonic and higher-harmonic excitations will appear.

The amplitude of a subharmonic at $\omega_m \approx 1/2, \ldots$, and a higher harmonic at $\omega_m \approx 2, \ldots$ can be obtained by the ansatz

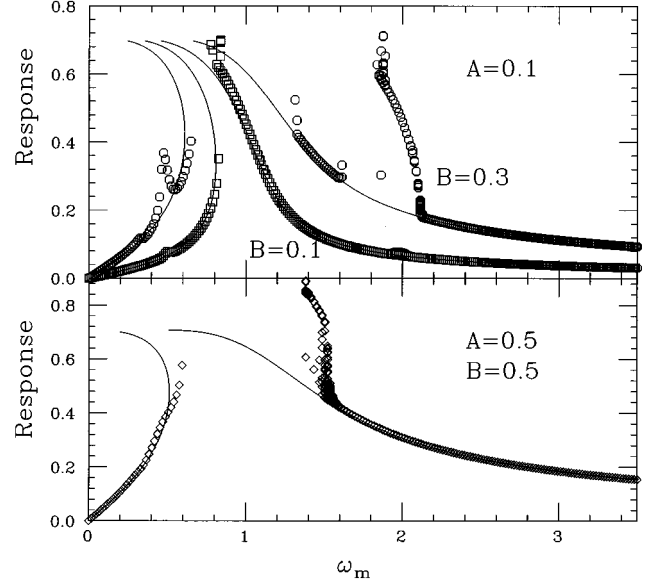FIG. 8. The amplitude of the steady state solution, called response, obtained numerically is plotted as a function of ω_m for $A=0.1$ (upper plot), with modulation amplitudes $B=0.1$ (rectangles), $B=0.3$ (circles), respectively, and for $A=0.5$ (lower plot) with $B=0.5$. Solid lines correspond to the solutions of Eq. (3.13). Two characteristic features shown in this figure are (1) the bifurcation threshold of the 2:1 parametric resonance is lowered by the friction force, and (2) a very strong stop band appears around $\omega_m=1$.

$$x(t) = X_0 + X_1\cos(\omega_m t - \chi_1) + X_2\cos(2\omega_m t - \chi_2), \quad (3.14)$$

$$x(t) = X_0 + X_1\cos(\omega_m t - \chi_1) + X_{1/2}\cos\left(\frac{\omega_m}{2}t - \chi_{1/2}\right), \quad (3.15)$$

respectively. For example, the subharmonic amplitude is given by

$$X_2 = \frac{X_1^2}{2[(4\omega_m^2 - X_1^2 - \sqrt{1-2X_1^2})^2 + 4\omega_m^2 A^2]^{1/2}}.$$

Such a procedure has been extensively tested in the study of many dynamical systems [14,15].

3. Relation between the periodic solution and the parametric resonances

A close relation exists between parametric resonances of the Hamiltonian system and periodic solutions of the damping system. When a friction term is added to the Hamiltonian system, the particle moves slower in the phase space and the tune of the system is lowered. At the same time, the 1:1 parametric resonance becomes more important so that the amplitude of particle oscillations becomes larger. This will also lower the bifurcation tune of the 2:1 resonance. The decrease of the threshold 2:1 resonance bifurcation tune is evident in the lower plot of Fig. 8, where the bifurcation tune of the 2:1 resonance is $\omega_m \approx 1.515$ for $A=0.5$ instead of

$\omega_m \approx 2.1$ for $A = 0.1$. Because the Mathieu instability has a finite width in the tune space, the bifurcation tune occurs at $\omega_m = 2.1$ instead of 2 for a small damping parameter A. Furthermore, SFPs of dominant parametric resonances become attractors while SFPs of weak parametric resonances are destroyed. In other words, periodic solutions of damped differential equations can be associated with the corresponding SFPs of strong parametric resonances in equivalent Hamiltonian systems, where a few strong parametric resonances survive to become attractors. If attractors exist, particles will damp to periodic solutions, or equivalently, SFPs of parametric resonances.

The characteristic phase oscillation tune for the attractor associated with a 2:1 parametric resonance is $\omega_m/2$. More generally, the attractor associated with the n:m parametric resonance will have an orbiting tune of $(m/n)/\omega_m$. For example, although the Poincaré surfaces of section for the 3:2 secondary resonance and the 3:1 primary resonance are similar, their time-dependent function is different. The primary 3:1 resonance has a time-dependent function of $\cos\frac{1}{3}\omega_m t$, while the 3:2 secondary resonance has a time-dependent function of $\cos\frac{2}{3}\omega_m t$. In the Poincaré surfaces of section, the difference can be visualized as follows: Particle motion in the 3:1 primary resonance will jump from an island to the immediate neighboring island consecutively. However, particles jump from one island to the next neighboring island at the secondary 3:2 resonance condition. Using such a signature, the role of parametric resonances in chaos can be identified. Since secondary resonances arising from 1:1 and 2:1 primary resonances overlap with each other, they provide the stochastic background for global chaos.

B. The 2:1 parametric resonance

The period-2 parametric resonance is known to play a crucial role in chaos. The route of chaos is usually presented by a vivid portrait of sequences of period-2 bifurcation. The period-2 bifurcation is related to the 2:1 parametric resonance or the Mathieu instability in a dynamical system [12]. For the nominal rf system with rf phase modulation, the resonance strength for the $n = 2$ parametric resonance is zero [13]. If the modulation frequency is near 2, i.e., $\omega_m \approx 2$, the $n = 2$ parametric resonance is important for a QI Hamiltonian. The Hamiltonian in the zero friction approximation is given by

$$H = H_0(J) + \frac{1}{2}\omega_m B g_2(J)\cos(2\psi - \omega_m t) + \Delta H(t),$$

$$(3.16)$$

where all incoherent time-dependent terms are lumped into $\Delta H(t)$. Using the resonance strength function of Eq. (2.35), and the generating function

$$F_2(\psi, J_1) = \left(\psi - \frac{\omega_m}{2}t\right)J_1,$$

the Hamiltonian can be expressed as

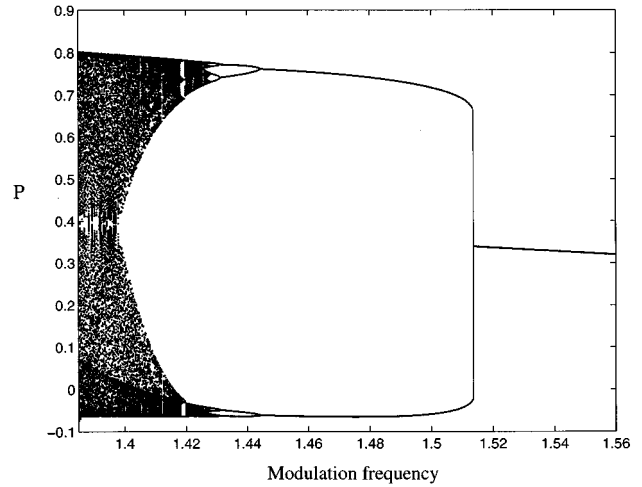$$H_{2:1} = H_0(J_1) - \frac{\omega_m}{2}J_1$$

FIG. 9. The phase space coordinate p of the attractor in the Poincaré surface of section is plotted as a function of the modulation frequency (tune) ω_m near the region of global chaos for parameters $A = 0.5$ and $B = 0.5$. Note that the phase space attractor bifurcates into two at the modulation tune of about 1.515. It follows a series of period-2 bifurcations before reaching global chaos at $\omega_m = (5 - \sqrt{5})/2$.

$$+ \frac{1}{2}\omega_m B g_2(J_1)\cos(2\psi_1) + \Delta H_{2:1}(t),$$

$$\approx \left(1 - \frac{\omega_m}{2}\right)J_1 - \frac{5}{12}J_1^2 + \omega_m f_2 J_1 \cos 2\psi_1 + \Delta H_{2:1}(t),$$

$$(3.17)$$

where $f_2 \approx \frac{1}{6}B(\pi/2K)^2$, and we have used a small amplitude approximation for the unperturbed time-independent Hamiltonian. The right plot of Fig. 5 shows an example of the Poincaré surface of section for the 2:1 parametric resonance. Since the time averaged Hamiltonian $\langle H_{2:1}\rangle$ of Eq. (3.17) has been extensively studied in Ref. [12], we will not repeat it here. It is worth mentioning that the remnant time-dependent term $\Delta H_{2:1}(t)$ plays the role of harmonic modulation to the tori of the primary 2:1 parametric resonance. Since the island tune $Q_{2:1}$ of the 2:1 primary parametric resonance has a characteristic similar to that of Fig. 2 (see Ref. [12] for analytic expression of the island tune), secondary parametric resonance islands within the primary resonance island can be created. This self-similar phenomenon provides the richness of the portrait of chaos.

C. Chaos through period-2 bifurcation

The path that dynamical systems undergo in order to develop global chaos is a fascinating subject. Figure 9 shows the phase space coordinate p of the Poincaré surface of section as a function of modulation frequency near the region of period-2 bifurcation with parameters $A = 0.5$ and $B = 0.5$. For $\omega_m \gtrsim 1.515$, there is only one attractor (see Figs. 8 and 9). When ω_m is varied below 1.515, two attractors suddenly appear in the phase space. Decreasing ω_m further, we find that four attractors appear in the phase space. The sequence of period-2 bifurcation continues until global chaos at $\omega_m \approx (5 - \sqrt{5})/2 = 1.381966$ is reached.
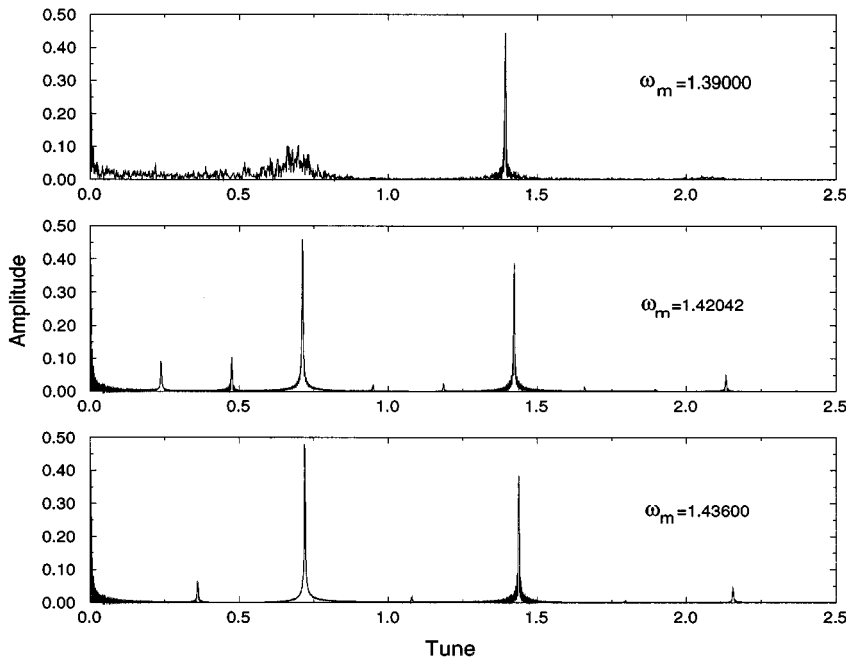
FIG. 10. The FFT spectra of steady state solutions with parameters $A=0.5$, $B=0.5$, and $\omega_m=1.39$ (top), 1.4204 (middle), 1.436 (bottom) are plotted.

Figure 10 shows the fast Fourier transform (FFT) spectra of steady state solutions for $A=0.5$, $B=0.5$, with $\omega_m=1.39$ (top plot), 1.4204 (middle plot), and 1.436 (bottom plot). The first period-2 bifurcation is associated with the occurrence of a $\frac{1}{2}$ harmonic in the FFT spectrum. This can be identified as the primary 2:1 parametric resonance. The second period-2 bifurcation corresponds to the appearance of a $\frac{1}{4}$ harmonic (see the bottom plot of Fig. 10). Occurrence of a $\frac{1}{6}$ harmonic in the route of global chaos is also evident from the FFT spectrum shown in the middle plot of Fig. 10. The FFT spectrum of global chaos has a characteristic of white-noise-like structure shown in the top plot of Fig. 10.

Figure 11 shows Poincaré surfaces of section with $A=0.5$, $B=0.5$, and $\omega_m=1.39$, 1.436, 1.48, and 1.54, respectively. At $\omega_m=1.54$, the system has a single attractor associated with a 1:1 parametric resonance. At $\omega_m=1.48$, the attractor bifurcates into two attractors, which are confirmed to be SFPs of the 2:1 parametric resonance. At $\omega_m=1.436$, each SFP of the 2:1 parametric resonance bifurcates into two attractors within the basin. At $\omega_m=1.39$, particles damp to attractors composed of fractal lines with no definite tune. This corresponds to the breakdown of the fixed point attractors within the basin of attraction for the 2:1 parametric resonances. It is also interesting to note that periodic attractors are located near the band of chaotic attractors shown in Fig. 11.

D. Transition to global chaos and Melnikov integral

We observed in the last few sections that the QI dynamics system would encounter global chaos when the modulation amplitude was large. What is the critical modulation amplitude for the onset of global chaos? A method of handling this estimation is the evaluation of the Melnikov integral.

The Melnikov integral method has often been applied to study the chaotic transition of many dynamical systems. If the stable and unstable orbits from a hyperbolic fixed point cross each other, the dynamical system becomes homoclinic, an indicator of chaotic motion. Calculating the distance between the stable and unstable orbits perturbatively, the Melnikov integral becomes [14]

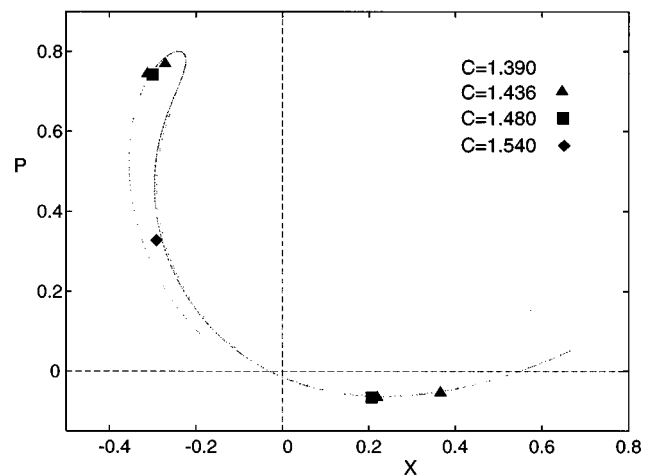$$D=-\int_{\infty}^{\infty}[\omega_m B p(t-t_0)\cos\omega_m t-Ap^2(t-t_0)]dt.$$

(3.18)

FIG. 11. The phase space map (p,x) of the Poincaré surface of section for steady state solutions with $A=0.5, B=0.5$ is shown. The parameter C is the modulation tune ω_m. The diamond symbol shows a single attractor at $\omega_m=1.54$ which is associated with the 1:1 parametric resonance. Rectangular symbols show the period-2 bifurcation, which is related to the 2:1 parametric resonance or Mathieu instability. Triangular symbols show attractors for the second period-2 bifurcation, which is unambiguously identified as the (2:1) secondary parametric resonance within the primary (2:1) resonance island. Dots correspond to the strange attractor with global chaos at $\omega_m=1.39$.
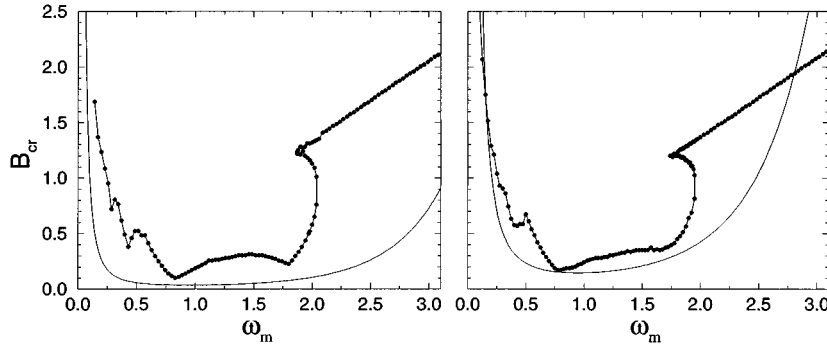
FIG. 12. The critical modulation amplitude B_{cr} is shown as a function of ω_m for $A = 0.05$ (left plot), and $A = 0.2$ (right plot). The symbols are obtained from numerical simulations, and the lines are obtained from the Melnikov integral method. Note that a cusp occurs at the transition of the 2:1 parametric resonance.

Using x and p of the separatrix orbit given by Eq. (2.27), the Melnikov integral for the Weierstrass $\wp$ equation becomes

$$D = 3\,\omega_m B \sin t_0 \int_{-\infty}^{\infty} \frac{\sinh t \, \sin \omega_m t}{(\cosh t + 1)^2} dt + 9A \int_{\infty}^{\infty} \frac{\sinh^2 t}{(\cosh t + 1)^4} dt$$

$$= + \frac{6\pi\omega_m^3 B \sin t_0}{\sinh \pi \omega_m} + \frac{6A}{5}. \tag{3.19}$$

The condition for global chaos becomes

$$B_{cr} = \frac{A}{5\pi} \frac{\sinh \pi \omega_m}{\omega_m^3}. \tag{3.20}$$

Based on the Melnikov integral method, the critical modulation amplitude B_{cr} for the chaotic condition is proportional to the damping parameter A. Since the ratio B_{cr}/A is at a minimum around $\omega_m \approx 1$, the system is most sensitive to external harmonic modulation near the first order synchrotron harmonic.

To verify the validity of the Melnikov integral estimation, we will perform some numerical simulations. Figure 12 shows the critical modulation parameter B_{cr} for the onset of global chaos as a function of ω_m, where the onset of global chaos is *defined* as the condition that the entire bucket is unstable. The estimation obtained from the Melnikov integral is also shown for comparison. We observe that the Melnikov integral provides a reasonable prescription for global chaos in the phase space. This agreement may result from the sharp drop of $Q(E)$ near the separatrix. However, the critical modulation amplitude B_{cr} obtained from numerical simulations shows a cusp at $\omega_m \approx 2$.

IV. SUGGESTIONS FOR EXPERIMENTAL OBSERVATION

There have been several low momentum compaction factor (low-α_c) experiments in synchrotron radiation light sources (see Ref. [6] for a review). Experiments in UVSOR in Japan and the SUPER-ACO in France have shown that if the second order momentum compaction η_1 was reduced, the first momentum compaction factor α_{c0} could be reduced by a factor of 100, resulting in a factor of 10 reduction in the bunch length at a low beam current. However, at high currents, experimental results seemed to indicate that the potential well distortion dominated the bunch length even in the low-α_c, or negative-α_c, regime. The experiments at the ALS further demonstrated that a bunch could split into sat-

ellite bunches [7]. Although detailed measurements of these satellite frequencies are not yet available, we believe that these satellite beamlets may arise from the 1:1 parametric resonance shown in the left plot of Fig. 5.

Based on our analysis, we would like to make the following suggestions for future low-α_c experiments. Since the bucket area of the QI Hamiltonian is proportional to $(V_0 |\cos\phi_s|)^{-1/2}$, QI experiments should study the beam stability at a lower rf voltage V with a large synchronous angle. In addition, since the effective damping coefficient is inversely proportional to ν_s, i.e., $A = \lambda/\nu_s$, and the stable phase space area increases with the damping parameter A, future experiments should examine the actual stable area. The stable phase space area can be studied through generating a phase kick to the beam and observing the survival of the beam particles. The rf phase noise is enhanced by the factor $\eta_1 / |\eta_0|^{3/2}$, and is hence a nuisance for QI storage rings. However, it is important to understand the effect of noise on particle dynamics. Carefully controlled experiments with rf phase modulation can be a step towards gaining more insight into the QI Hamiltonian system.

V. CONCLUSION

In conclusion, we have transformed the synchrotron equation of motion in the QI regime into a universal Weierstrass equation with the solution expressed in Jacobian elliptic functions. The phase space coordinates have been expanded in action-angle variables. The expansion coefficients, commonly known as the strength function, play an important role in determining the strength of parametric resonances resulting from rf phase or voltage noise. We have also shown that the strength function vanishes at the center of the bucket and the separatrix, and that higher-harmonic parametric resonances in the QI dynamical system are much more important near the separatrix. Thus it is easier to attain chaos for this dynamical system.

We have also found that the effective damping force for the QI Hamiltonian is inversely proportional to $|\eta_0|^{1/2}$, hence making the effective damping force larger in QI storage rings. The damping force can increase the stable phase space area and distort the "phase space ellipse." However, we have also shown that the effective rf phase modulation amplitude is proportional to $|\eta_0|^{-3/2}$, and thus particularly enhanced in the QI regime. The effects of rf phase modulation can induce many parametric resonances. When a weak damping force is included, the stable fixed point of the parametric resonance becomes an attractor which is also the

TABLE II. Fixed points of the nonlinear synchrotron Hamiltonian.

	ϕ	δ	Characteristics
Nominal fixed points	0	0	SFP
	$\pi - 2\phi_s$	0	UFP
Nonlinear compaction	$\pi - 2\phi_s$	$-\eta_0 / \eta_1$	SFP
Fixed points	0	$-\eta_0 / \eta_1$	UFP

steady state solution of the differential equation. The beam particles will damp to attractors and form multiple bunches orbiting about the center of the bucket. It is possible that the satellites observed in Ref. [6] correspond to beamlets in the 1:1 parametric resonance islands.

As the damping force gets stronger, the phase space becomes distorted. We have demonstrated that the steady state solution can be well approximated by the harmonic linearization method. When the modulation amplitude was also large, our numerical simulations showed that the system exhibited chaos through a series of period-2 bifurcations, where a strange attractor occurred near the onset of global chaos. The Melnikov integral method was also found to provide a reasonable but not accurate prediction for the onset of chaos.

ACKNOWLEDGMENTS

APPENDIX A: THE SYNCHROTRON HAMILTONIAN

Using (ϕ, δ) as conjugate phase space coordinates, where ϕ is the rf phase angle and δ is the fractional momentum deviation from the synchronous particle, synchrotron mapping equations are given by

$$\delta_{n+1} = \delta_n + \frac{eV}{\beta^2 E}[\sin(\phi_{n+1} + \phi_s) - \sin\phi_s] - 2\pi\lambda\,\delta_n,$$
(A1)

$$\phi_{n+1} = \phi_n + 2\pi h(\eta_0 \delta_{n+1} + \eta_1 \delta_{n+1}^2),$$
(A2)

where the subscript stands for the revolution number, V is the rf voltage, h is the harmonic number, ϕ_s is the synchronous phase, η_0, η_1 are linear and nonlinear phase slip factors, and λ is the damping decrement. Neglecting the friction term, the difference equation can be cast into the Hamiltonian given by

$$H = \frac{1}{2}h\,\eta_0 \delta^2 + \frac{1}{3}h\,\eta_1 \delta^3 + \frac{eV}{2\pi\beta^2 E}[\cos(\phi + \phi_s) + \phi \sin\phi_s],$$
(A3)

where $\theta = s/R$ serves as the time coordinate, and R is the mean radius of the storage ring. The fixed point of this Hamiltonian is given by Table II.

For a regular rf bucket, the maximum bucket height is given by

$$\hat{\delta} = \left(\frac{2eV}{\pi\eta_0 E}\left[\left(\frac{\pi}{2} - \phi_s\right)\sin\phi_s - \cos\phi_s\right]\right)^{1/2}.$$
(A4)

Transition from the nominal rf bucket to the ''α bucket'' occurs when the separatrix of these two buckets merge into one [2], i.e.,

$$\left|\frac{\eta_0}{\eta_1}\right| \leqslant \hat{\delta}.$$
(A5)

In the QI regime, where $|\eta_0 / \eta_1| \ll \hat{\delta}$, the Hamiltonian can be approximated by

$$H = \frac{1}{2}h\,\eta_0 \delta^2 + \frac{1}{3}h\,\eta_1 \delta^3 - \frac{eV\cos\phi_s}{4\pi\beta^2 E}\phi^2,$$
(A6)

where Hamilton's equation of motion becomes

$$\dot{\delta} = \frac{eV\cos\phi_s}{2\pi\beta^2 E}\phi, \quad \dot{\phi} = h\,\eta_0 \delta + h\,\eta_1 \delta^2,$$
(A7)

or

$$\ddot{\delta} + \nu_s^2 \delta + \frac{\eta_1}{\eta_0}\nu_s^2 \delta^2 = 0,$$
(A8)

where

$$\nu_s = \sqrt{\frac{heV|\eta_0 \cos\phi_s|}{2\pi\beta^2 E}}, \quad \eta_0 \cos\phi_s \leqslant 0$$
(A9)

is the small amplitude synchrotron tune. Now, we define the phase space coordinate x and the new time coordinate t as

$$x = -\frac{\eta_1}{\eta_0}\delta, \quad t = \nu_s \theta.$$
(A10)

Then the synchrotron equation of motion becomes

$$x'' + x - x^2 = 0,$$
(A11)

where the prime corresponds to the derivative with respect to the time coordinate t. Letting

$$p = x' = \frac{\eta_1 \nu_s}{\eta_0^2}\phi$$
(A12)

be the conjugate momentum to the coordinate x, the Hamiltonian for the QI storage rings becomes

$$H = \frac{1}{2}p^2 + \frac{1}{2}x^2 - \frac{1}{3}x^3,$$
(A13)

where (x, p) are conjugate phase space variables.

Defining the action variable as

$$J = \frac{1}{2\pi}\oint p\,dx,$$
(A14)

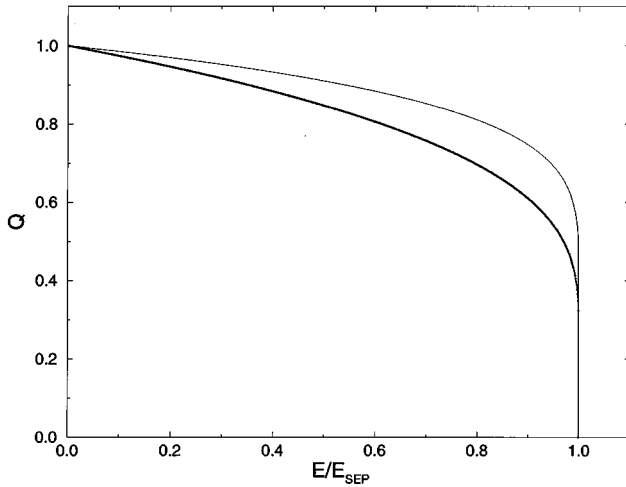the area in (ϕ, δ) phase space is given by

FIG. 13. The normalized synchrotron tunes $Q = Q_s(E)/\nu_s$ for the QI Hamiltonian (thin line) and the nominal synchrotron Hamiltonian (thick line with dots) are shown as a function of the normalized energy E/E_{sep}.

$$\mathcal{A} = \oint \phi\, d\delta = \left(\frac{\eta_0^{5/2}}{\eta_1^2} \right) \left(\frac{2\pi h \beta^2 E}{eV|\cos\phi_s|} \right)^{1/2} 2\pi J. \quad \text{(A15)}$$

The bucket area is obtained by substituting the action of the separatrix orbit which gives

$$\mathcal{A}_B = \frac{6}{5} \left(\frac{|\eta_0|^{5/2}}{|\eta_1|^2} \right) \left(\frac{2\pi h \beta^2 E}{eV|\cos\phi_s|} \right)^{1/2}. \quad \text{(A16)}$$

Note here that the bucket area increases as the rf voltage V and $|\cos\phi_s|$ decreases. The constraint $eV\sin\phi_s = U_0$ is needed to compensate energy loss due to synchrotron radiation.

1. Synchrotron tunes of the QI and nominal rf Hamiltonian

The difference in the amplitude dependence of the synchrotron tunes for the QI Hamiltonian and the nominal rf Hamiltonian plays an important role in the particle dynamics. Figure 13 shows the normalized synchrotron tune $Q_s(E)/\nu_s$ vs the normalized energy E/E_{sep} for the QI Hamiltonian (thin line) and the nominal synchrotron Hamiltonian (thick solid line with dots). In particular, we note that the synchrotron tune for the QI Hamiltonian drops sharply to zero at the separatrix, which causes many parametric resonances to overlap one another. Thus the QI dynamical system is much more sensitive to harmonic modulation than the nominal rf Hamiltonian.

2. Phase space damping

In the presence of the phase space damping, the equation of motion is given by

$$\ddot{\delta} + \nu_s^2 \delta + \frac{\eta_1}{\eta_0} \nu_s^2 \delta^2 + \lambda \dot{\delta} = 0, \quad \text{(A17)}$$

where $\lambda = J_E U_0/(2\pi E_0)$ is the damping decrement, $J_E \approx 2$ is the damping partition number for synchrotron phase space, and U_0 is the energy loss per revolution. Table III lists some typical parameters of storage rings, where LEP, HERB, APS,

CESR, and ALS stand respectively for the large electron positron collider at CERN, the high energy ring of the B factory design at SLAC, the advanced photon source at Argonne National Laboratory, the Cornell electron storage ring, and the advanced light source at the Lawrence Berkeley National Laboratory

Expressing the equation of motion in the normalized phase space coordinates, we obtain

$$x'' + x - x^2 + Ax' = 0, \quad \text{(A18)}$$

where the normalized damping coefficient is given by

$$A = \frac{\lambda}{\nu_s}. \quad \text{(A19)}$$

The parameter A for some non-QI-electron storage rings is listed in Table III. We note that A is relatively small for nominal momentum compaction lattices. On the other hand, if the momentum compaction factor α_{c0} is lowered by a factor of 100, the effective damping parameter will increase by a factor of 10. We thus choose to study $A \in [0,0.5]$.

3. rf phase modulation Hamiltonian

When the synchrotron tune of a QI lattice becomes smaller, the system may become much more susceptible to the rf phase noise. In the presence of the phase modulation, the equation of motion is given by

$$\ddot{\delta} + \nu_s^2 \delta + \frac{\eta_1}{\eta_0} \nu_s^2 \delta^2 = \nu_m a \cos\nu_m \theta, \quad \text{(A20)}$$

where ν_m is the modulation tune, and a is the phase modulation amplitude. Using the normalized phase space coordinates, the equation of motion becomes

$$x'' + x - x^2 = -\omega_m B \cos\omega_m t, \quad \text{(A21)}$$

where $\omega_m = \nu_m/\nu_s$, and the effective modulation amplitude becomes

$$B = \frac{\eta_1}{\eta_0 \nu_s} a. \quad \text{(A22)}$$

Thus the effective phase modulation amplitude, proportional to $|\eta_0|^{-3/2}$, is greatly enhanced due to the smallness of the first order phase slip factor $|\eta_0|$.

TABLE III. Typical parameters of electron storage rings.

	LEP	HERB	APS	CESR	ALS
E_0 (GeV)	55	9	7	6	1.5
U_0/E_0 (units of 10^{-3})	4.8	0.39	0.78	0.32	0.074
α_{c0} (units of 10^{-4})	3.9	24.4	2.4	152	14
ν_s	0.085	0.05	0.0066	0.064	0.0082
A (damping)	0.018	0.0024	0.037	0.002	0.003
f_0 (kHz)	11.2	136	283	390	1524
f_{syn} (kHz)	0.956	6.8	1.9	25	12.5

APPENDIX B: RELATION BETWEEN THE WEIERSTRASS $\wp$ FUNCTION AND JACOBIAN ELLIPTIC FUNCTION

The Weierstrass function satisfies the equation

$$\left(\frac{d\wp(u)}{du}\right)^2 = 4(\wp - e_1)(\wp - e_2)(\wp - e_3). \quad \text{(B1)}$$

Letting $\wp = e_3 + (e_2 - e_3)\sin^2 z$, the Weierstrass equation becomes

$$\int_0^w \frac{dz}{\sqrt{1 - m\sin^2 z}} = \int_0^u \sqrt{e_1 - e_3}\, du = \sqrt{\frac{e_1 - e_3}{6}}\, t, \quad \text{(B2)}$$

where

$$m = \frac{e_2 - e_3}{e_1 - e_3}.$$

By the definition of the Jacobian elliptic function, the solution $\wp$ is given by

$$\wp = e_3 + (e_2 - e_3)\sin^2 w = e_3 + (e_2 - e_3)\,\text{sn}^2\left(\sqrt{\frac{e_1 - e_3}{6}}\, t \,\middle|\, m\right). \quad \text{(B3)}$$

APPENDIX C: SUM RULES

Using the generating function of Eq. (2.22), we obtain the coordinate transformation

$$d\psi = Q\frac{dx}{p}. \quad \text{(C1)}$$

Thus the sum rule of Eq. (2.37) becomes

$$S_p(J) = \frac{1}{2\pi}\int p^2 d\psi = \frac{Q}{2\pi}\oint p\, dx = QJ. \quad \text{(C2)}$$

Substituting the equation of motion $x'' + x - x^2 = 0$ into Eq. (2.38), one obtains

$$S_x = \frac{1}{2\pi}\int x^2 d\psi = \frac{1}{2\pi}\int (x'' + x)d\psi = \frac{1}{2\pi}\int x\, d\psi = g_0. \quad \text{(C3)}$$

---

[1] C. Pelligrini and D. Robin, Nucl. Instrum. Methods Phys. Res. Sect. A **301**, 27 (1991).

[2] D. Robin, E. Forest, C. Pelligrini, and A. Amiry, Phys. Rev. E **48**, 2149 (1993); H. Bruck *et al.*, IEEE Trans. Nucl. Sci. **NS20**, 822 (1973).

[3] L. Liu *et al.*, Nucl. Instrum. Methods Phys. Res. Sect. A **329**, 9 (1993).

[4] H. Hama, S. Takano, and B. Isoyama, Nucl. Instrum. Methods Phys. Res. Sect. A **329**, 29 (1993); S. Takano, H. Hama, and G. Isoyama, Jpn. J. Appl. Phys. **32**, 1285 (1993).

[5] A. Nadji *et al.*, in *Proceedings of the Fourth European Particle Accelerator Conference*, edited by V. Suller and Ch. Petit-Jean-Genaz (World Scientific, Singapore, 1994), p. 128.

[6] D. Robin, H. Hama, and A. Nadji, Lawrence Berkeley Laboratory Report No. LBL-37758, 1995 (unpublished).

[7] D. Robin *et al.*, Stanford Linear Accelerator Center Report No. SLAC-PUB-95-7015, 1995 (unpublished).

[8] D.F. Lawden, *Elliptic Functions and Applications, Applied Mathematical Sciences* (Springer-Verlag, New York, 1989),

Vol. 80.

[9] *Handbook of Mathematical Functions*, edited by M. Abramowitz and I.A. Stegun (National Bureau of Standards, Washington, DC, 1975).

[10] I.S. Gradshteyn and I.M. Ryzhik, *Table of Integrals, Series, and Products* (Academic Press, New York, 1980).

[11] S.Y. Lee *et al.*, Phys. Rev. E **49**, 5717 (1994); J.Y. Liu *et al.*, *ibid.* **50**, R3349 (1994); J.Y. Liu *et al.*, Part. Accel. **49**, 221 (1995).

[12] D. Li *et al.*, Phys. Rev. E **48**, R1638 (1993); Nucl. Instrum. Methods Phys. Res. Sect. A **364**, 205 (1995).

[13] H. Huang *et al.*, Phys. Rev. E **48**, 4678 (1993); M. Ellison *et al.*, Phys. Rev. Lett. **70**, 591 (1993); M. Syphers *et al.*, *ibid.* **71**, 719 (1993); Y. Wang *et al.*, Phys. Rev. E **49**, 1610 (1994).

[14] T. Kapitaniak, *Chaotic Oscillations in Mechanical Systems* (Manchester University Press, Manchester, 1991).

[15] G. Rega, in *Bifurcation and Chaos*, edited by J. Awrejcewicz, Springer Series in Nonlinear Dynamics (Springer, Heidelberg, 1995), p. 191.